Discover Chemistry

RESEARCH Open Access

Characterization and electrochemical analysis of aluminium-citrate ion cell from waste aluminum foils and natural citric acid

John Wamumwe Mwangi[1,2*], Denis Kiragu[3], Bakari Chaka[4] and James Ndiritu[5]

*Correspondence:
John Wamumwe Mwangi
d.mvangi@g.nsu.ru
[1]Department of Natural Sciences, Novosibirsk National Research State University, Novosibirsk, Russia
[2]Boreskov Institute of Catalysis, Novosibirsk, Russia
[3]Department of Chemistry, Benue State University, Makurdi, Benue, Nigeria
[4]Department of Mathematics and Physical Sciences, Maasai Mara University, Narok, Kenya
[5]Department of Biological and Physical Sciences, Turkana University College, Lodwar, Kenya

Abstract

This study aims to prepare an aluminum-citrate ion cell from waste aluminum foils and citric acid extracted from *Dovyalis caffra* fruits (Kei apples) and further demonstrate their electrochemical performance at varying impedances, electrode thicknesses and discharge times. Aluminum oxide ions were prepared from discarded aluminum foils, and citric acid were produced by co-precipitating macerated *Dovyalis caffra* extracts by acid infusion. Aluminum foil wastes were utilized in acid co-digestion to produce aluminum oxide nanoparticles. The prepared aluminum oxide was then characterized for surface morphology, composition and phases present. The prepared particles revealed Al_2O_3 boehmite moieties and ranged between 66.3 and 106.1 nm in size. The synthesized citric acid depicted desirable morphological and electrolytes traits similar to those of commercial citric acid. The cells open and closed current-voltages were directly proportional to the electrode diameter. While the cells were found to be quite Ohmic in nature with increased impedance with electrode distances, discharge times were also proportional to electrode diameters. The cell's energy balance was 477.6–346.3 J/s, with a density of 47.1–53.7 Wh/kg. The results showed that the cells could successfully produce portable energy storage devices from waste materials.

Keywords Aluminum foil waste, Aluminum oxide nanoparticles, Aluminum oxide cell, Citric acid

1 Introduction

The demand for energy storage materials has constantly increased with increasing energy requirements [1]. Aluminum ion cells are suitable and effective energy storage devices with a wide range of applicability and are environmentally safe. Their energy densities and discharge rates are compatible with most loads. The contemporary state-of-the-art raw materials for the fabrication of aluminum ion cells are quite expensive, especially in developing nations, thus limiting its production in these countries [2]. This has made the cells expensive and out of reach to many residents in developing nations.

On the other hand, there are significant aluminum wastes for fabrication of aluminum ion cells [3].

The production lines of the aluminum industry and end-of-life products are the two primary sources of aluminum trash [4]. Recycling is a good alternative in both situations and is used extensively in industrialized nations. This is however not the case in developing countries. According to Siddiqua et al. [5], aluminum waste that builds up in landfills is a solid waste hazard that can harm the immune system, cause skin conditions, cause liver damage, and cause some types of cancer. This supports the need for more environmentally friendly ways to recycle aluminum.

Unlike lithium-ion batteries, where the mobile ion is Li^+, aluminum forms a compound with chloride in most electrolytes and produces an anionic mobile charge transporter, usually $AlCl_3^-$ or $Al_2Cl_3^-$ [6]. The total amount of energy or power a battery can release depends on factors including the battery cell's voltage, capacity, and chemical composition [7]. A battery can maximize its energy output levels [8] by increasing chemical potential charge between the two electrodes, reducing the mass of reactants and preventing the electrolyte from being improved by the chemical reactions.

Modern aluminum ion cells have used various chloride electrolytes, including ammonium chloride, magnesium chloride, HCl acid, and 1-ethyl-3-methylimidazolium chloride (EMIC), among many others [9]. Because of their complementarity with Al^{3+} which facilitates easy charge transfer between the electrodes, chloride ions are more favored [10]. During charge and discharge cycles, these cells demonstrated excellent Al^{3+} electrochemical deposition at the anode and chloroaluminate anion ($AlCl_4^-$) intercalation in the cathode [11]. Citric acid's luxuriance to metal ions, in addition to its high dissociation constant, K_a, has shown promise for electrolytic behavior [12, 13]. Citrate ions' ($C_3H_5O(COO)^{3-}$) trivalent nature better complements Al^{3+}. Citric acid can be extracted with inexpensive, readily available chemicals under mild conditions. Therefore, using citrate ions as electrolytes and taking advantage of the electrochemical behavior of aluminum ion cells is desirable. In this work, aluminum foils were used as the electrodes to create and evaluate a citrate-aluminum ion cell.

2 Materials and chemicals

2.1 Materials

The aluminum ions were derived from waste aluminum foils, while citrate ions were obtained by co-precipitation of *Dovyalis caffra* macerated extracts followed by acid infusion. All chemicals used (hydrochloric acid, sodium carbonate, potassium bromide, citric acid) were analytical grade (all > 99% purity level) and were sourced from Sigma-Adrich (Germany).

2.2 Synthesis and characterization of Al_2O_3 nanoparticles

To obtain aluminum oxide nanoparticles, purified waste aluminum foils were gradually scrubbed on the surface to remove any oxide coating before being digested with 1 M HCl acid (35% v/v) at room temperature. After effervescence, the Al_2Cl_3 digestate was thoroughly washed with running distilled water (equal volume) and co-precipitated with an equivalent aliquot of 0.5 M sodium carbonate solution, as shown in Eq. (1) [10].

$$2Al_2Cl_3\,(s) + 2Na_2CO_3\,(aq) \rightarrow 2CO_2\,(g) + 2Al_2O_3\,(s) + 6NaCl\,(aq) \quad (1)$$

The residue was allowed to settle before being thoroughly washed and decanted to remove the sodium chloride. The mixture was filtered to obtain aluminum oxide, which was then dried for 3–4 h in an oven at 100 °C to remove water. Mechanical milling was then used to reduce the particles to the desired nanoparticle range using various pore-sized sieves using a pulverizer (Retsch BB 500 (Germany) jaw crusher, mouth width 250 × 130 mm, feed grain size up to 110 mm and a fineness of 90% < 0.5 mm). The obtained white solid was thoroughly rinsed with distilled water to reduce impurities. X-ray fluorescence (XRF) analysis was used to confirm the purity of the samples until a threshold impurity concentration of 10% was obtained.

The presence of functional groups in the samples were investigated using FTIR spectroscopy (Shimadzu 119, Japan). The FTIR spectra of the samples were recorded in the transmittance mode in the range of 4000–500 cm^{-1} [14]. The crystallinity, particle size, and polymorphs of the formed nanoparticles were determined using X-ray diffraction (XRD-7000, Shimadzu). Milled powder samples will be placed on steel sample holders and leveled to achieve total and uniform X-ray exposure. The samples were then analyzed at room temperature (25 °C) using a monochromatic CuK radiation source (λ = 0.1539 nm) in step-scan mode with a 2θ range of 10° to 80°, a step of 0.04 units, and a scanning time of 5.0 min. The size of the crystals was determined by the Scherrer formula (Eq. 2) [14];

$$D = K\lambda/\beta\cos\theta \tag{2}$$

where D is the crystal particle size (nm), λ is the X-ray beam wavelength, K is the constant (0.94), β is the peak width at half maximum intensity, θ and is the peak position used to calculate the crystallite size. The morphological appearance of the samples was observed using scanning electron microscopy (SEM) (VEGA3, TEGSCAN). The images were captured at an operating voltage of 5 kV and a Robinson backscatter detector. A Field Emission Scanning Electron Microscope (FE-SEM) was used to capture the images. The samples were coated with gold sputtering prior to imaging. EDS (FEI XL40 ESEM equipped with two EDAX Sapphire Si (Li) EDS detectors and MLA software) was used to determine the samples' elemental composition.

2.3 Extraction and characterization of citric acid

Dovyalis caffra contains of 3, 4, 5-trimethoxycinnamic acid which ferments to citric acid as shown in Eq. 3 [15]. *Dovyalis caffra* fruits were washed with distilled water and shade-dried for 72 h at room temperature. The fruits were then mechanically blended and filtered by a 3 mm sieve followed by a 1 mm sieve to ensure smooth pulp without skin or fiber and left to ferment for 2 days. The fruits sap was squeezed out and then filtered several times using a clean cotton cloth. The filtrate was centrifuged at 200 rpm for 2 h and the supernatant was stored at 10℃ for 24 h. The solution was then diluted five-folds in distilled water before concentrating in a rotor evaporator to obtain solid citric acid. The citric acid produced was confirmed by morphological and physico-chemical analysis.

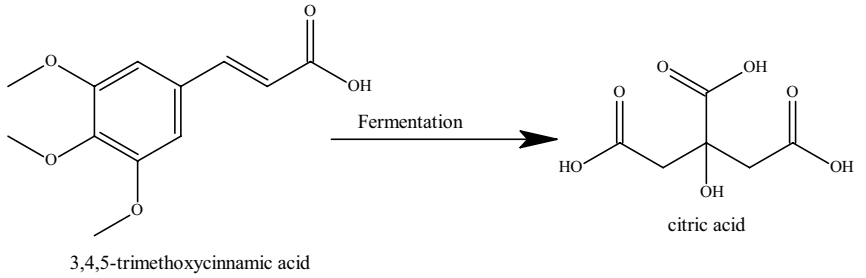

(3)

2.4 Electrode preparations and assembly of fabricated aluminum-citrate ion cell

A graphite rod (SFG6L) was used to make the anode while the cathode was varied between standard and the synthesized Al_2O_3 nanoparticles. Two commercial conductive binders i.e. Silicone adhesive (SA) and Polyacrylate Adhesive (PA) were used to enjoin the particles onto the supporting rod (graphite) in the ratio of 90:10 (Al_2O_3: Adhesive). Graphite was preferred for its ability to improve the reversible charge density and electrode adhesion for favorable industrial processability. The Al_2O_3 nanoparticles suspended between the electrolyte and the electrodes were gradually kneaded for around 20 min between 20 and 30°C and stirred at 400–500 rpm. The suspension was then left overnight under room pressure (1 atm) and cast on pure aluminium (Korff AG, Switzerland) with a thickness of 22 μm as a current collector to yield the electrode. The electrodes were manually calendared with room pressure (1 atm) and molded in the cuboid shapes to obtain workable compact electrodes. The aeral mass loading rate was 20 $mgcm^{-3}$. An electrode length of 49 ± 5 mm, external diameter 5.0 ± 0.5 mm was arrived at. The aluminium ion cell was fabricated using a cuboid polymeric insulator (dimensions 130 mm by 220 mm base area and height 100 mm). Citric acid electrolyte was used for each setup, three sets of different electrode diameters were used i.e. 2.0, 3.0 and 5.0 mm.

2.5 Cell performance tests

Electrochemical performance of the cell was established and all the voltage readings were recorded using a multi-meter (Model: UT33B; DC Voltage: 200mV, 2000mV, 20V, 200V ± (0.5% + 2)/500V ± (0.8% + 2); AC Voltage: 200V/500V ± (1.2% + 10) and DC Current (A)) at room temperature (25°C) and pressure. The resistance of the multi-meter during the closed-circuit voltage experiments was 100Ω. The performance of the synthetic aluminium oxide nanoparticles was compared with those of standard aluminium oxide nanoparticles (Catalog Number, ACM11092323-61; CAS 11092-32-3) using the citric acid electrolyte.

Electrochemical measurements were done at varying electrode distances to monitor the cell performance under varying impedance. A graphite anode of similar volume to the cathode one was constantly used for all the experiments while the cathode electrode diameter was varied. The three cathode variations used were labelled as 1, 2 and 3 and each had diameters of 2 mm, 3 mm and 5 mm respectively. The Energy capacity and densities values were obtained as indicated in Eqs. (4) and (5). The energy capacity was calculated by dividing the energy balance (in J/s) with the cell volume (Eq. 4). The energy density was calculated by dividing the energy capacity by the weight of the cell (Eq. 5)).

The specific gravity of citric acid electrolyte used were the theoretical values of 1.24 g/ml [16].

$$\text{Energy capacity} = (\text{Energy balance})/(\text{Cell Volume}) \tag{4}$$

$$\text{Energy density} = (\text{Energy capacity})/(\text{Cell gravimetric weight}) \tag{5}$$

2.6 Data analysis

Statistical analysis was performed using Origin (Version 2018), Microsoft Excel (version 2016) and Graphpad Prism 9.5.0 (730) for Windows (Prism, USA). Correlations were considered to be statistically significant at a 95% confidence interval ($P < 0.05$).

3 Results and discussion

3.1 X-ray diffraction (XRD) studies

The data from the diffractogram obtained (Fig. 1) were compared to the database of the Joint Committee on Powder Diffraction Standards (JCPDS) card file No. 46-1215 outlined by David [13], which confirmed the crystalline structure of the synthesized Al_2O_3 nanoparticles.

There were four main polymorphs associated with alumina nanoparticles: α, θ, γ, and κ observed in the diffractogram [17]. The polymorphic phase change is associated with changes in critical lattice parameters such as particle diameter and density [18]. The samples examined revealed the presence of Al_2O_3 nanoparticle crystal phases and traces of elemental aluminum. The Al_2O_3 polymorphs were observed for the sample's larger peaks, 32.72° and 59.46°. These phases are known to exist at lower temperatures [10]. The α-Al_2O_3 phase were observed at 45.66° [10]. Annealing Al_2O_3 by gradual oxidation causes the growth of the otherwise naturally amorphous layer of Al_2O_3 [14].

The kinetics of the reactions are governed by the outward diffusion of alumina ions [2]. During the process, a critical thickness layer distinguishes the Al_2O_3 phases. As a result of the polymorph and critical layer growth (5 nm), the latter phase is larger. Further growth of the polymorph results in the formation of Al_2O_3 [19]. The Al_2O_3 polymorphs are the smallest, most stable, and dense [20]. This phase is obtained after continuous oxidation of the Al_2O_3, which is accompanied by inner grain boundary diffusion of oxygen anions [21]. This inward shift is responsible for the relatively more compact -Al_2O_3.

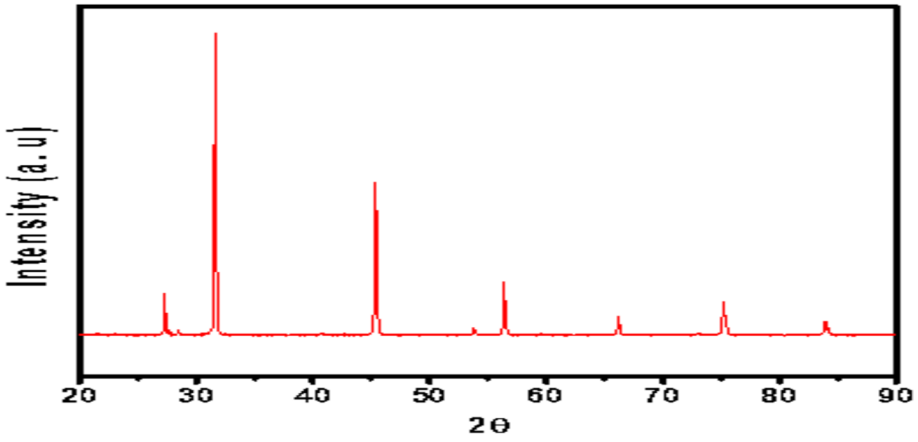

Fig. 1 XRD spectrum of the synthesized Al_2O_3 nanoparticles

The indices of the major peaks in the diffractogram were matched as follows: 2θ [32.72°, 46.53°, 67.80°, and 77.01°]. The highest peak intensity was observed at angle $2\theta = 32.72°$. The peak corresponded to $-Al_2O_3$ as well as boehmite crystal structures with octahedral and orthorhombic bipyramidal shapes [22].

The presence of Al_2O_3 and boehmite geometry revealed that the compound was not pure. This could be attributed to the origin of the alumina. Al_2O_3 structures has desirable characteristics for use as a battery electrode, such as good water release patterns, slow polymerization, and condensation pathways [23, 24]. Most boehmite-based compounds are also optically active [25]. The calculated size of this crystal (using the Scherrer equation) was 63.763 nm. The other prominent peak was found at $2\theta = 45.68$. This peak corresponded to a rhombohedral crystal structure (lattice parameters a = 4.76 and b = 12.99), which were discussed theoretically [24].

3.2 Microstructure of the synthesized Al_2O_3 nanoparticles

The SEM micrographs of the prepared Al_2O_3 nanoparticles are as illustrated in Fig. 2. The micrographs indicated a uniform material with unevenly spread specs. The spectra are an indication of partial oxidation on the surface of the electrodes due to the high reactivity of aluminium with oxygen in ambient conditions [26]. Agglomerates of the spots were also observed and this was alluded to particle clustering during synthesis and handling. Agglomeration reduces the effective surface area available for electrochemical reactions, thus hindering the performance of the electrodes. Grain boundaries were quite visible at a resolution of 100 µm. The grain boundaries were also unevenly spread out. While the boundaries potentially hinder charge transfer during electrolysis [27], they also provide larger surface areas and more active sites for electrochemical reactions, which can benefit electrode performance in terms of capacitance and charge storage [28]. The electrode micrographs indicated clustered and distinct particles when

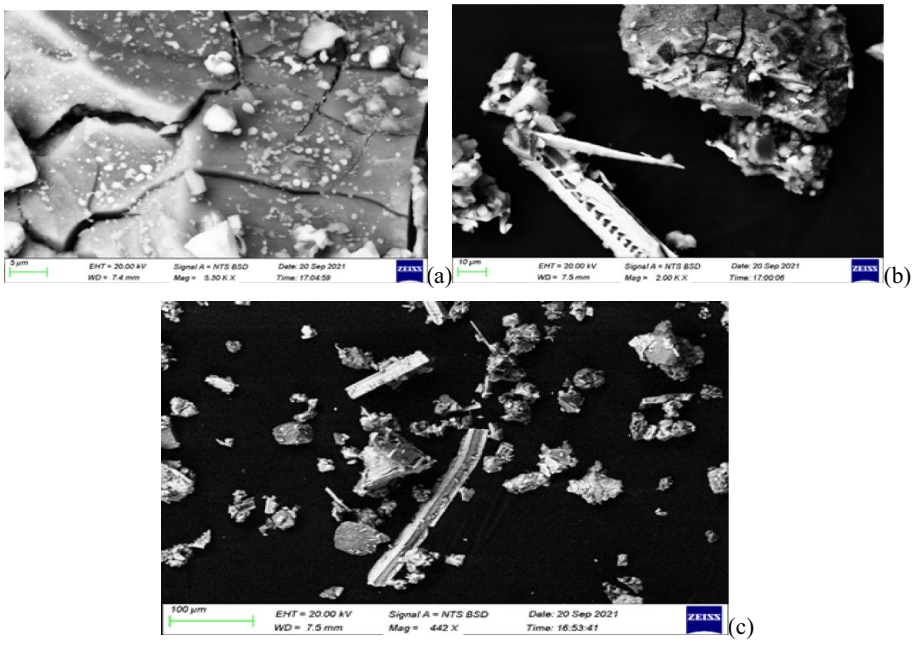

Fig. 2 Microstructure of the of aluminum oxide as observed under scanning electron microscopy (SEM) under different resolutions i.e. 5 µm (**a**), 10 µm (**b**) and 100 µm

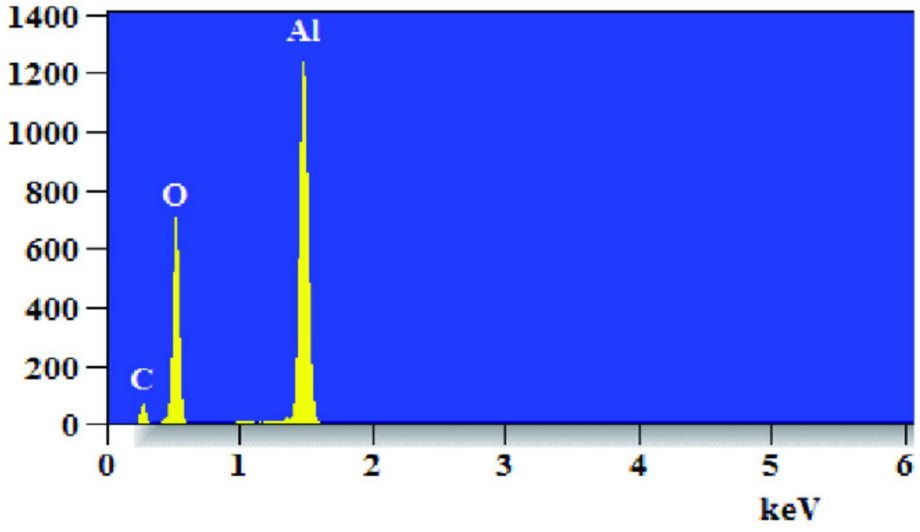

Fig. 3 The EDS spectrum of the prepare Al_2O_3 nanoparticles

Table 1 Percentage composition of the major elements detected

Elements	Weight %	Atomic %
Al K	65.87	60.07
O K	25.51	27.65
C K	8.62	12.28
Total	100	

viewed at a larger resolution (10 and 100 µm) (Fig. 3b, c) with the void sites due to be filled with electrolyte solution during the cell performance. The micrographs indicated that the Al_2O_3 nanoparticles were well prepared for optimal cell performance.

Figure 2 also depicts the surface morphology of aluminum oxide, which was irregularly shaped.

3.3 Chemical composition determination

The chemical composition of aluminum oxide nanoparticles was analyzed using EDS as indicated in Fig. 3. The quantitative measuring results were used to reflect the purity of the prepared aluminum oxide nanoparticles. The results indicated presence of Al^{3+} and O^{2-} ions as the most prevalent ones, as well as carbon signals in the samples arising from the precursor reagents used in the preparation of the nanoparticles. The dominant Al^{3+} and O^{2-} peaks is an indication of the sample's high purity levels. Table 1 shows the percentage of the major elements detected.

3.4 Functional group analysis of the Al_2O_3 nanoparticles

FT-IR spectrum of the prepared Al_2O_3 nanoparticles is illustrated in Fig. 4. The correlation of the absorption bands (vibrational bands) and the chemical compounds in the sample is part of the IR spectrum evaluation [24]. Cl^- vibrational bonds were observed at 406 and 432 cm^{-1} [24]. The peaks were due to the product NaCl solution used in preparation of the samples. Al–O stretching peaks were also observed at 584 cm^{-1} indicatives of the bonds in the prepared nanoparticles [25]. This was further affirmed by the Al–O vibration peaks at 830 cm^{-1}, characteristic of boehmite alumina [25]. The peak

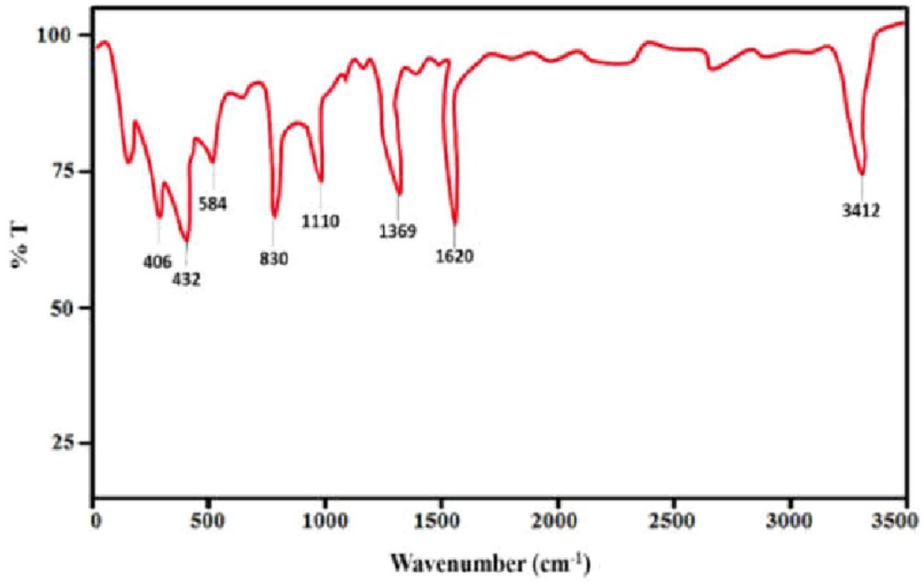

Fig. 4 FT-IR spectrum of aluminum oxide nanoparticles

Table 2 Physio-chemical parameters of the prepared electrolyte at 284.4 K and 1 atm

Parameter	Mean	Std Dev
Acidity (H^+)	1.83	0.022
Dissolved oxygen (%)	3.97	0.515
Conductivity (S/m)	1.15	0.362

at 1110 cm^{-1} indicates the triply degenerative vibrational mode of chloro group. The samples also exhibited traces of impurities peaks such as ester C=O stretching vibration peaks at 1369 cm^{-1}. There were traces of olefin impurities as illustrated in the bending vibration of water molecules adsorbed on a surface due to the C=C stretching vibration at 1620 cm^{-1}.

Presence of water molecules bending and stretching vibration modes were further observed with the peaks at 3412 cm^{-1}. The spectrum indicated the need for more purifications to reduce the effectiveness of these impurities and water molecules in the electrochemical performance of the electrodes.

3.5 Characterization of the prepared electrolyte (citric acid)

3.5.1 Physical–chemical parameters of the electrolyte

From Table 2, the mean pH of the extracts was recorded to be 1.83 ± 0.022. The pH value was due to the extract's precursor matrix that involved other acids such as ascorbic acid, tartaric acid, malic acid, and other impurities. This composition makes the pH of acid lower than the actual pH, which ranges between 3 and 6. Table 2 also indicated that the synthesized citrate ions were a good conductor of electricity with an electrical conductivity of 1.15 S/m; thus, can act as a good electrolyte because it dissociates completely. Low values of specific conductance are characteristic of high-quality, oligotrophic (low nutrient) in *Dovyalis caffra* [25, 26]. A multi-purpose portable physico-chemicals kit (Hanna P-114) was employed to determine the dissolved oxygen concentration in the extracts.

The above results in Table 2 imply that the compound is bonded with oxygen molecules as shown in Eq. (3). Dissolved oxygen concentration is another important factor influencing battery cell performance [27] which have can be reduced by Inert Atmosphere Gloveboxes where the Battery electrolyte is handled and assembled in gloveboxes filled with inert gases like argon or nitrogen. This prevents oxygen from the air from coming into contact with the sensitive materials.

3.5.2 Functional group analysis

Figure 5 show the FT-IR spectrum of citric acid extracted from *Dovyalis caffra*. The samples closely resembled standard citric acid in all the key functional groups. There were quite a number of peaks in the fingerprint region of the samples owing to the acid extract and the precursor organic matrix peaks. This was due to overlapping and distinct peaks from these two sources combine to create a crowded and information-rich fingerprint region, reflecting the diverse chemical composition of the analyzed samples [24]. The peak at 1030 cm^{-1} indicated a C–O stretching vibration peaks characteristic of most acids. The stretching of C–O peak was also observed at 1260 cm^{-1} illustrating presence of –C–O–H group in the extracts [24]. There was also a carbonyl group at a wavelength of 1496 cm^{-1}, which implies the presence of a carboxylic acid group, confirming acidity. The carbonyl group (C=O) stretching vibration, specifically associated with esters and ketones, were also observed at 1750 cm^{-1}.

The presence of a large, broad peak spanning the region between 3000 and 3500 cm^{-1} in Fig. 5 is a strong indicator of the vibrational stretching modes of both O–H bonds in hydroxyl groups and the –C–O–O–H bonds within carboxylic acid groups.

3.6 Electrolytic properties of fabricated aluminium-citrate ion cell

The physical–chemical parameters of the fabricated cell were assessed for essential parameters that would potentially affect the cell performance as indicated in Table 3. Based on the data in Table 3, pH was found to be 4.42, the oxygen dissolved was 3.3 mg/L, and the conductivity was 1.45 S/cm. The acidity reported (pH 4.42) for the aluminum oxide can be attributed to the amphoteric nature of the oxide. As the pH increases, the conductivity increases due to the increased amount of delocalized hydrogen ions, and

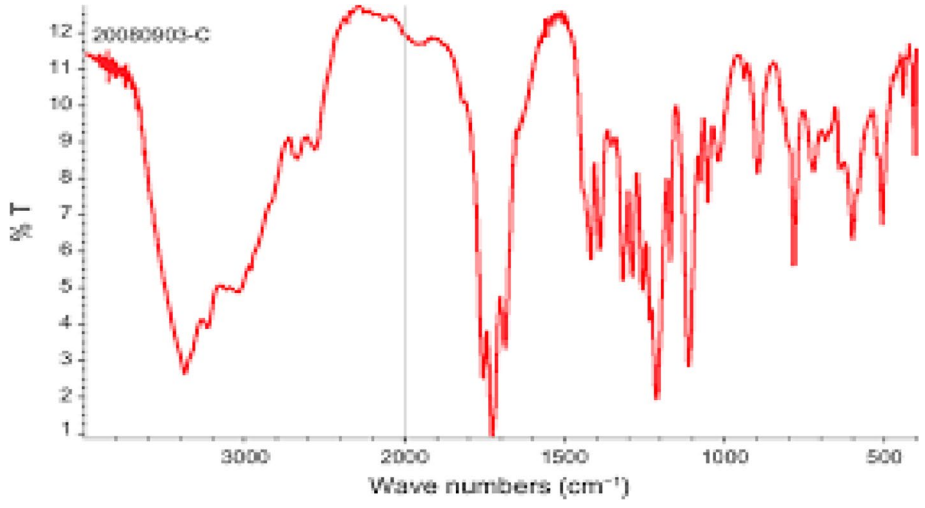

Fig. 5 FT-IR spectrum of the extracted citric acid

Table 3 Physical–chemical measurements at a temperature of 284.4 K and 1 atm

Parameter	Readings							Mean	Std Dev
Acidity (H^+)	4.5	4.47	4.44	4.42	4.39	4.35	4.34	4.42	0.098
Dissolved oxygen (mL/L)	3.9	3.8	3.6	3.1	2.8	2.6	2.4	3.3	0.602
Conductivity (S/m)	1.7	1.5	1.4	1.2	1.1	0.9	0.7	1.45	0.348

this furthers the mobility of hydrogen ions, which consequently increases with increase in concentration [28]. The increase in H^+ concentration affects the production of current and voltage, raising the efficiency of the ion cell.

The cell had 3.3 ± 0.544 of dissolved oxygen fundamental in supply of oxygen for electrochemical oxidation as well as stabilization of electrolytes. The average content of dissolved oxygen in such batteries is typically low, often around 0.5 to 20% by volume [29], as higher concentrations can lead to undesirable reactions that affect the battery's longevity and overall efficiency. Maintaining this low oxygen environment is crucial for optimal performance, preventing issues like electrolyte degradation or parasitic side reactions that can consume active materials and reduce the battery's lifespan. Therefore, rigorous control over the manufacturing process and sealing of these batteries is essential to minimize oxygen ingress and ensure the intended electrochemical processes proceed without detrimental interference from dissolved oxygen. The higher values of dissolved oxygen are due to the aqueous media used in preparation of both the electrodes and the electrolytes. Lower values of oxygen dissolved thus necessitate regular monitoring of the cells for enhancing the operational stability and life span of aluminum oxide batteries. The electrolyte's conductivity in aluminum ion cell is pivotal for enabling the movement of ions between the cathode and anode, thus facilitating the electrochemical reactions. Typically, the average conductivity for suitable electrolytes in such batteries ranged from 1 to 10 S/m [30], depending on the specific additives and temperature conditions. The cell conductivity of 1.45 ± 0.208 S/m was thus within the required range. The physical–chemical parameters indicated the cell composition were well balanced to enhanced electrochemical performance.

3.7 Open and closed-circuit voltage (OCV & CCV)

Open Circuit Voltage (OCV) there is no voltage generated within an aluminium ion cell meaning no electric current flows between the anodes and cathodes. In theory, because voltage losses do not impact OCV, it is anticipated to be equivalent to the electromotive force (emf). However, experimental studies reveal that voltage losses do indeed cause a notable decrease in the OCV value [31].

A closed voltage circuit is a complete pathway through which electric current can flow, allowing the voltage source to drive the movement of charge. The graph in Fig. 6 clearly demonstrates that as both resistance and distance increase, the voltage decreases. The voltage is very high at 0 resistance, and minimal voltage is produced at 10 ohms' resistance. This is due to an increase in internal resistance since the material is Ohmic [32]. The potential difference in this battery decreases due to increased electrode distance. Although the electromotive force remains constant, the resistance increases from 0 Ω to 1 Ω, 2 ohms, 5 ohms, and 10 ohms. As the electrode distance increases, the amount of current also decreases because of the increase in resistance electrode distance. At impedance levels of 5 and 10 ohms, there was a minimal change in voltage observed. This is because as resistance increases, the flow of electrons encounters more opposition

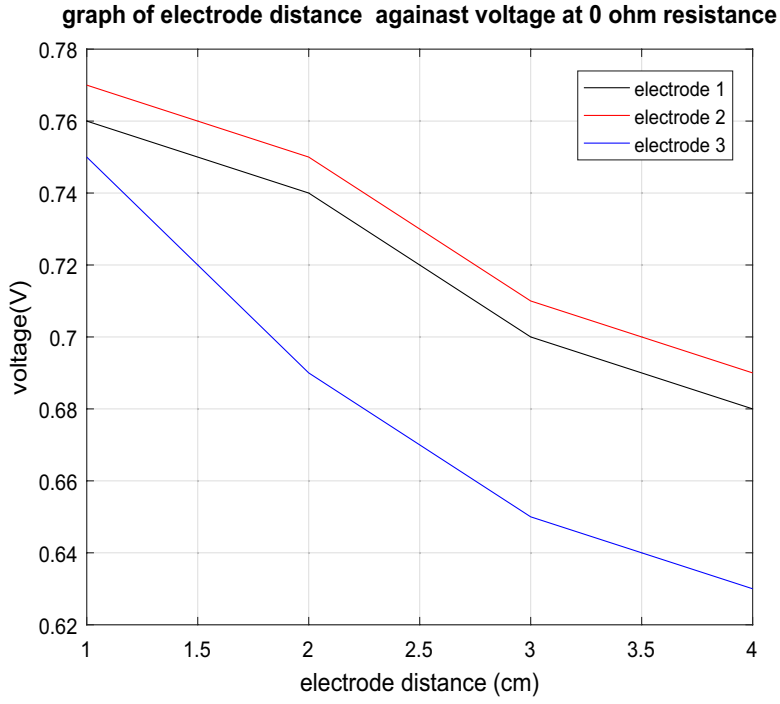

(a)

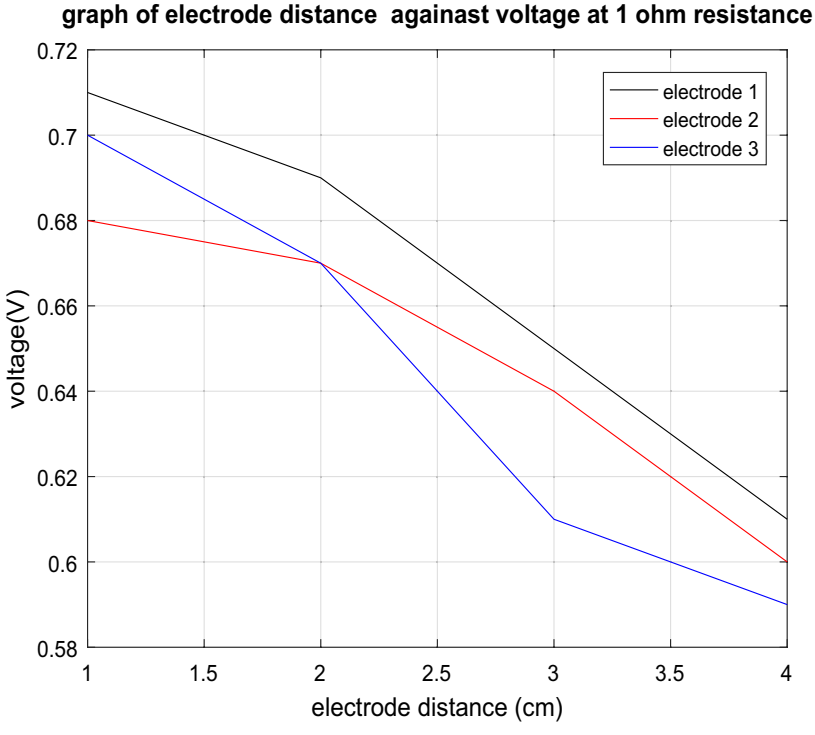

(b)

Fig. 6 Closed circuit voltage (where **a** is 0 Ω, **b** is 1 Ω, **c** is 2 Ω, **d** is 5 Ω, and **e** is 10 Ω. Resistors were used. Where electrode 1, 2 and 3 had diameters of 2, 3 and 5 mm, respectively)

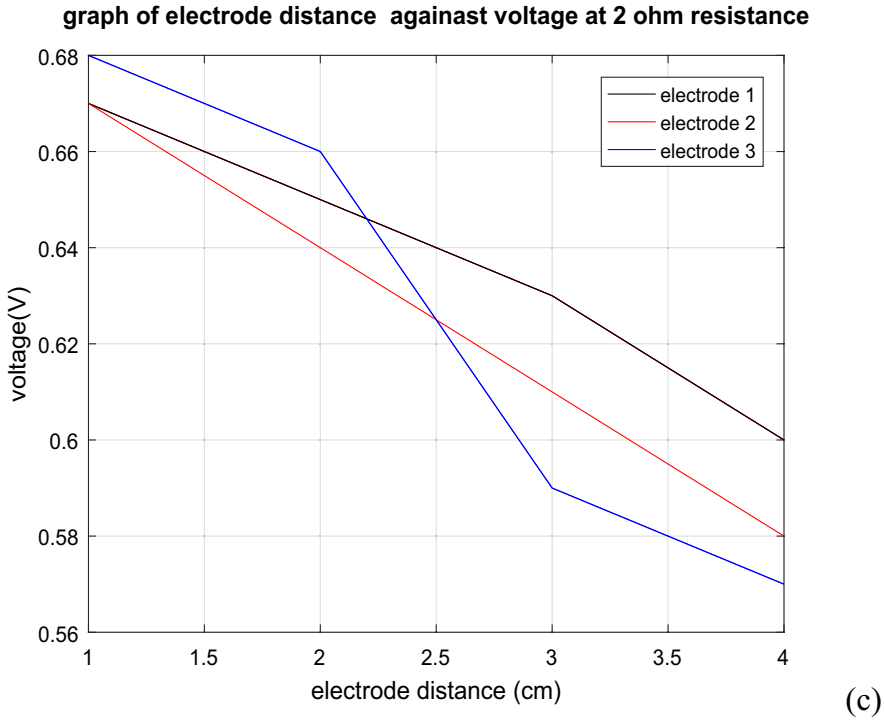

(c)

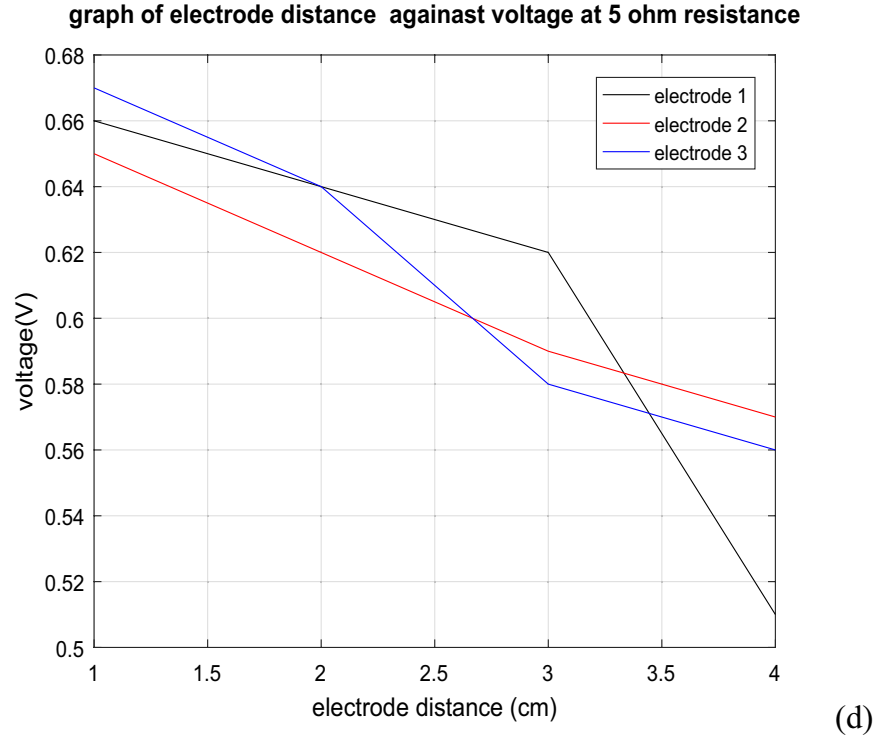

(d)

Fig. 6 (continued)

within the material. This opposition leads to more frequent collisions between the moving electrons and the atoms of the material (including any impurities). These collisions convert some of the electrical energy into thermal energy, generating heat. The amount of heat generated can be influenced by both the resistance and the presence of

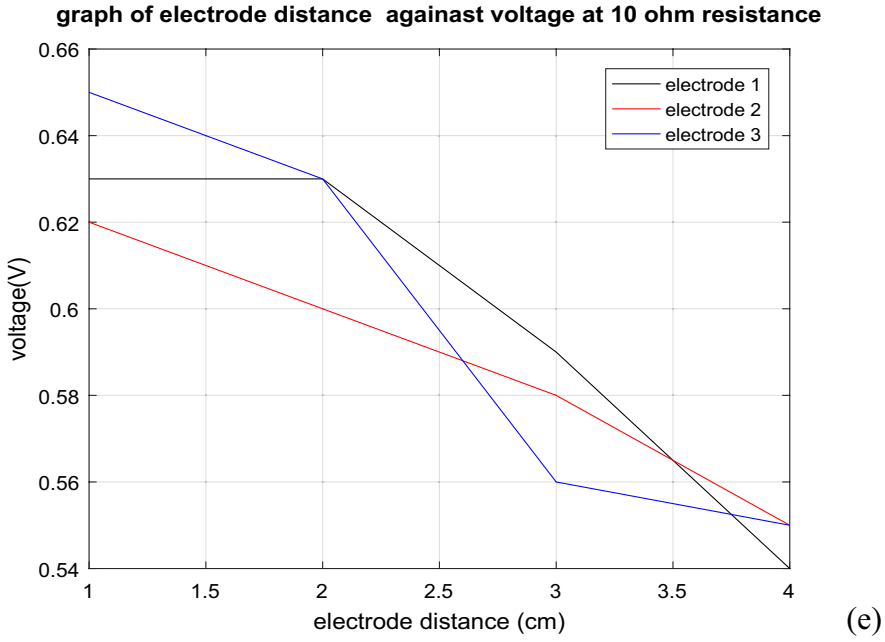

Fig. 6 (continued)

impurities, which can increase the likelihood of collisions and thus the energy lost as heat. The more impurity there is, the more heat will be produced. The amount of heat produced due to collision causes vibration of molecules, which increases resistance that causes low voltage [33].

As the electrode distance increases the voltage and current decreases due to the larger distance traveled by the electrons and this scenario can be well explained by the fact that the length of electrode is increasing from 1 to 4 cm [34]. The citric acid electrolyte, while facilitating ion transport, may become less effective under high resistance conditions, causing potential polarization effects and reducing the overall voltage supply.

3.7.1 Discharge rates (without a load)

From Fig. 7 the discharge rate was determined at a fixed electrode of length 3 cm, where the discharge rate was measured when there was no further change in current flowing and therefore time and voltage was recorded. There were two observations were made: one was that the resistance increased as the voltage decreased due to an increase in internal energy, the second one is that as time increases, the discharge rate increases due to reduced concentration of the analyte.

$$\mathrm{E_{cell}} = \frac{0.0591}{n}\log\frac{C1}{C2} \tag{6}$$

where n is the number of moles, C_1 and C_2 are the concentration of the analyte.

As the time increases, the concentration of the analyte decreases because fewer reactant particles are moving together [36]. Since these particles are responsible for conductivity, there will be a minimal current and voltage as the time increases, as depicted in Fig. 7. As the resistance also increases with an increase in time, the amount of current and voltage decreases simultaneously, which shows that the discharge rate slows down

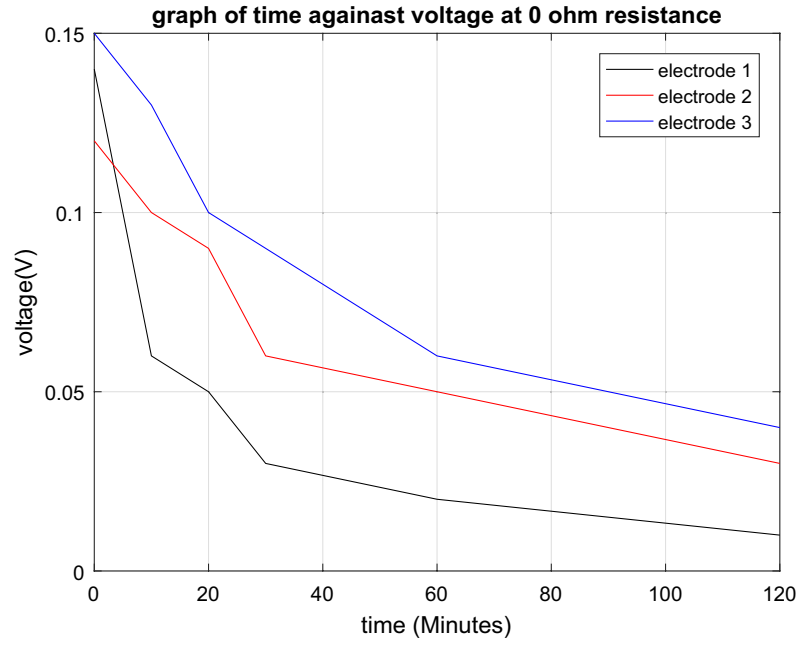

(a)

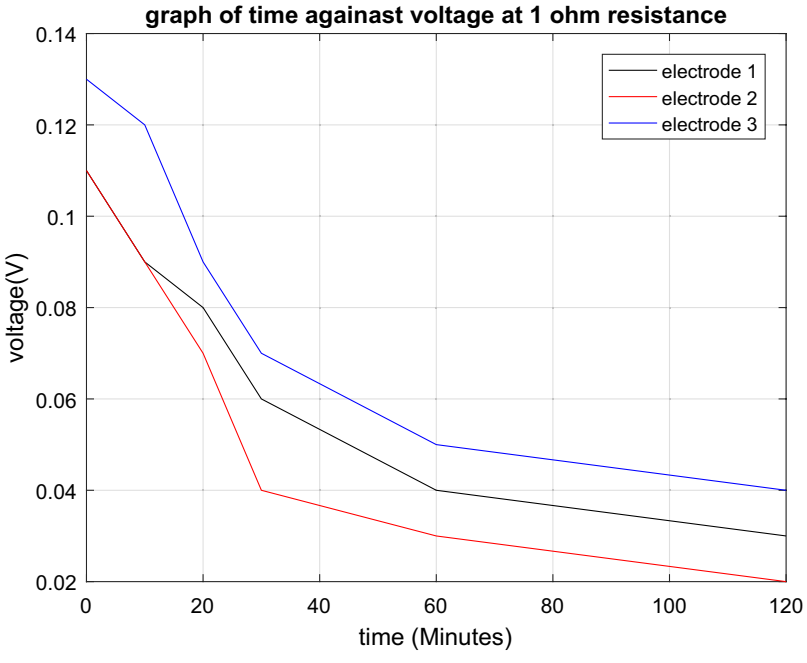

(b)

Fig. 7 Discharge Rates without a load (where **a** is 0 Ω, **b** is 1 Ω, **c** is 2 Ω, **d** is 5 Ω, and **e** is 10 Ω, Resistors were used. Where electrode 1, 2 and 3 had diameters of 2, 3 and 5 mm respectively). The amount of voltage and current increases due to an increase in concentration, as shown below by Eq. (6) [35];

over time in an electrochemical process where resistance builds up due to decrease in concentration of analyte [37].

3.7.2 Discharge rate (with a load)

The discharge rate with a load was measured at a constant electrode distance of 3 cm, a bulb is connected to the circuit and discharge voltage and time is recorded when the bulb goes off as shown in Fig. 8. The light lit dimly when a load was introduced (LED

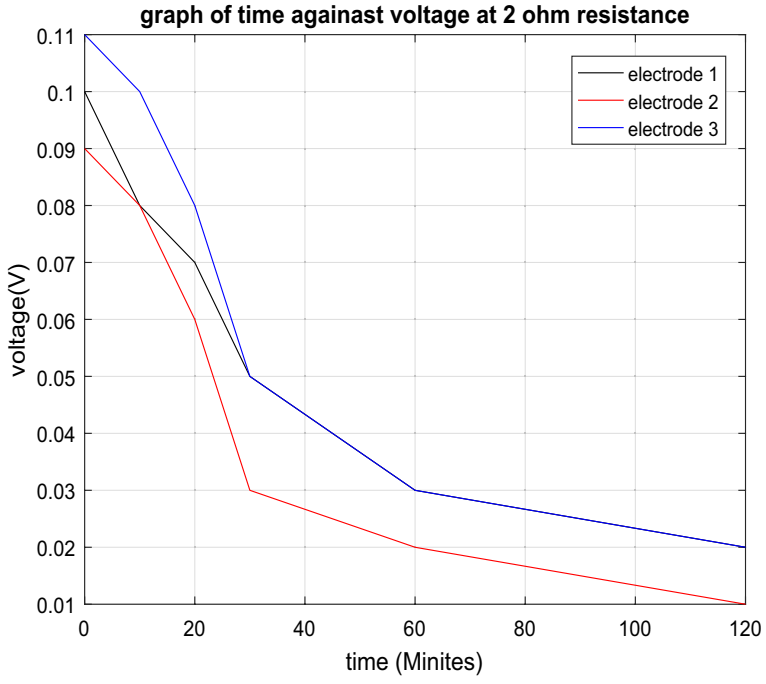

(c)

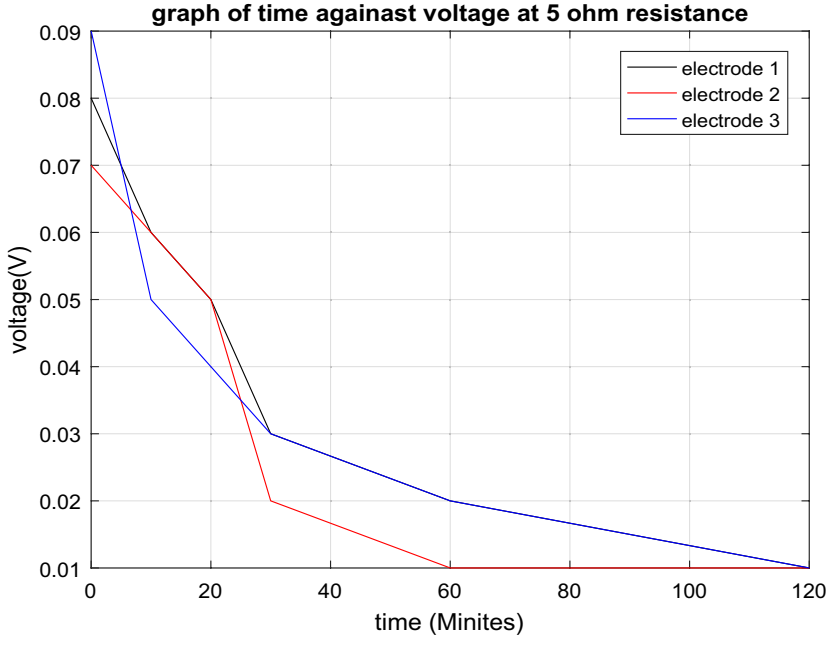

(d)

Fig. 7 (continued)

bulb, as the resistance, discharge time increased, the bulb light diminished due to an increase in internal resistance (The resistance to the flow of charge within a source) and a decrease in discharge rate, which was facilitated by a decrease in concentration and an increase in resistance. The conductivity is also high when the electrolyte concentration is high, and the resistance is small. As the time duration increases, there is less movement of particles in the electrolyte [38].

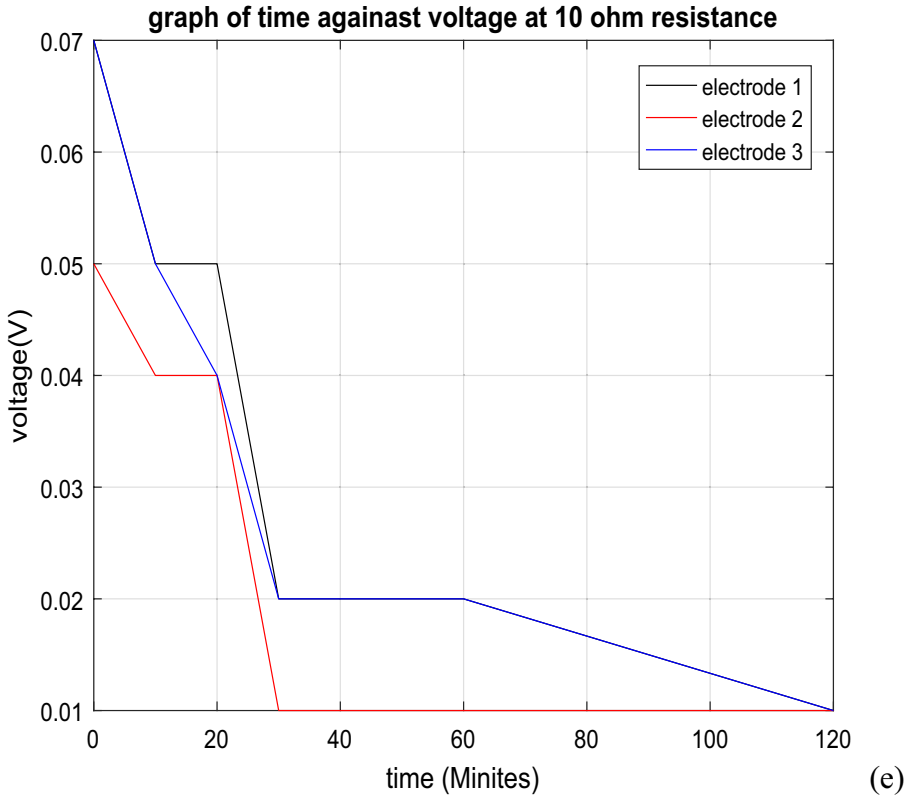

Fig. 7 (continued)

3.7.3 Change in electrolyte parameters

Figure 9a of pH against time shows that as time increases, the pH decreases because of a decrease in ion concentration because of the dissociation of citric acid due to release of H^+. Citric acid is 90% in proportion in *Dovyalis caffra* fruit extract [39]. On the other hand, in the second plot. Figure 9b of conductivity against time, the conductivity decreased due to a decrease in ion concentration, consequently reducing the number of mobile electrons, which are the charge carriers. Another citric acid factor is a weak electrolyte that does not dissociate altogether, leaving some unionized electrons.

3.7.4 Change in electrode parameters

As the time of reaction increases, and the diameter of the electrodes as shown in Fig. 10, keeps increasing due to the increase in reaction rate, thus causing the accumulation of reacting species ions on the surface of the electrodes.

An increase in the diameter of electrodes indicates that the reaction is taking place and there is the production of current and voltage [40]. The density increases due to the increase in the electrode's mass and decrease of the electrolytic volume due to its consumption. Since density is directly proportional to mass and inversely proportional to voltage and current, as the density of electrode increases, the electrolyte concentration decreases. The conductivity decreases due to the decrease in the concentration of mobile ions. Conductivity increases as concentration increases and density decreases.

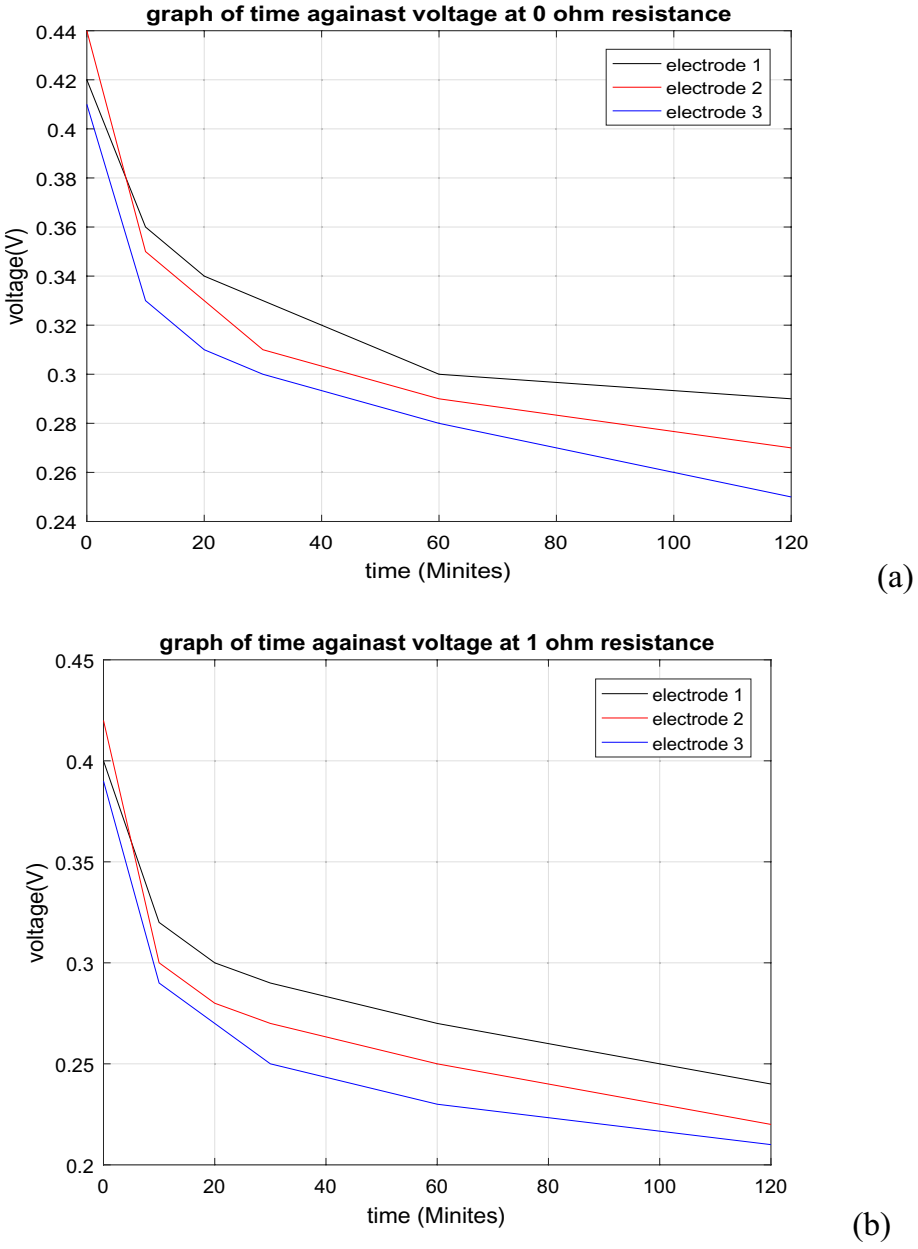

Fig. 8 Discharge rates with a Load (Bulb) load (where **a** is 0 Ω, **b** is 1 Ω, **c** is 2 Ω, **d** is 5 Ω, and **e** is 10 Ω, Resistors were used. Where electrode 1, 2 and 3 had diameters of 2, 3 and 5 mm respectively)

3.8 Variation in energy densities of the fabricated cell

The energy balance of cell is crucial in determination of the appliances to be used based on their weights and are a function of the cell density, columbic and voltage efficiency [41, 42]. The energy balance of the cells was found to increase linearly with magnitude of the electrode diameter. The cells State of Charge (SOC) have a direct impact on their voltage efficiency as well as energy balance. Thiong'o et al. [43] notes that such cells whose voltage varies linearly with the SOC are likely to have less voltage efficiency. From Table 4, the cell with a larger electrode diameter had more energy balance implying less Columbic efficiency. This indicated the ratio of charge input/output was lower in the cell with an electrode diameter of 2 mm and was thus the more stable electrode [44]. The

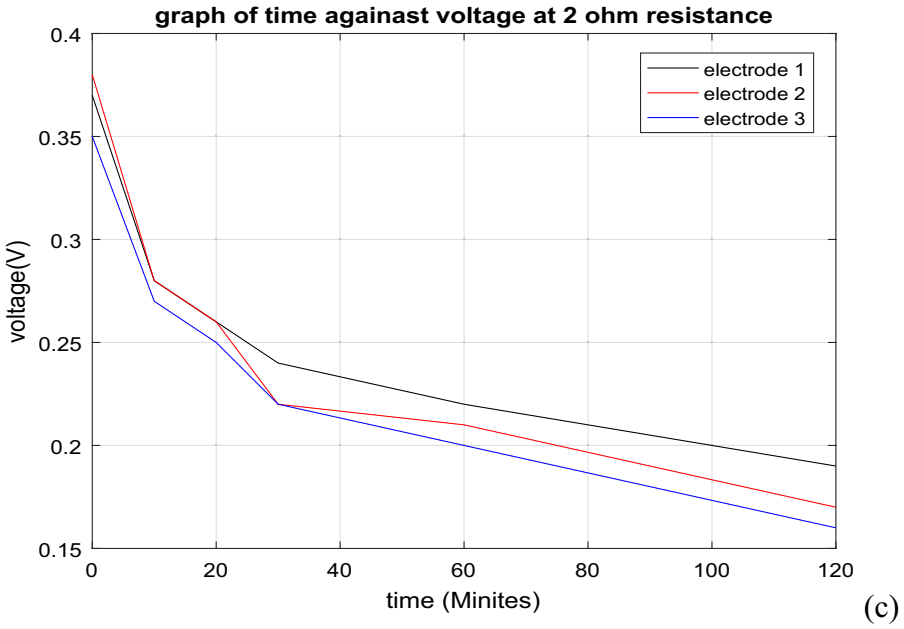

(c)

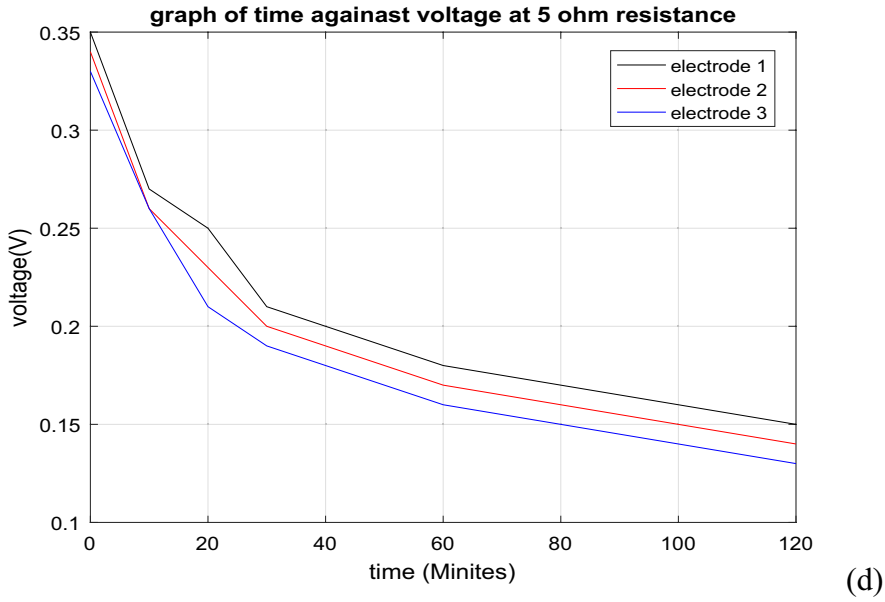

(d)

Fig. 8 (continued)

portrayed energy balance range (477.6 to 546.7 J/s) indicates strong potential for these cells for several domestic, industrial appliances and emerging grid storage solutions [45]. The gravimetric energy density is well within the expected one of 40 to 60 h/kg as observed in other Al-ion cells [46–48]. The deviation in energy balance and corresponding energy capacities with electrode diameter is as a result of increased Al_2O_3 ions availability for electrochemical reactions and Faradaic current with the increase in electrode diameters. The gravimetric and volumetric energy densities of the cells were well below the theoretical values (2980 mAh/g for the aluminum anode and 8046 mAh/cm^3 for the cathode) [49] owing from differences in the operating conditions.

The energy densities in Table 4 imply that the fabricated cells are light enough to for portable device while producing adequate energy to power several electric appliances.

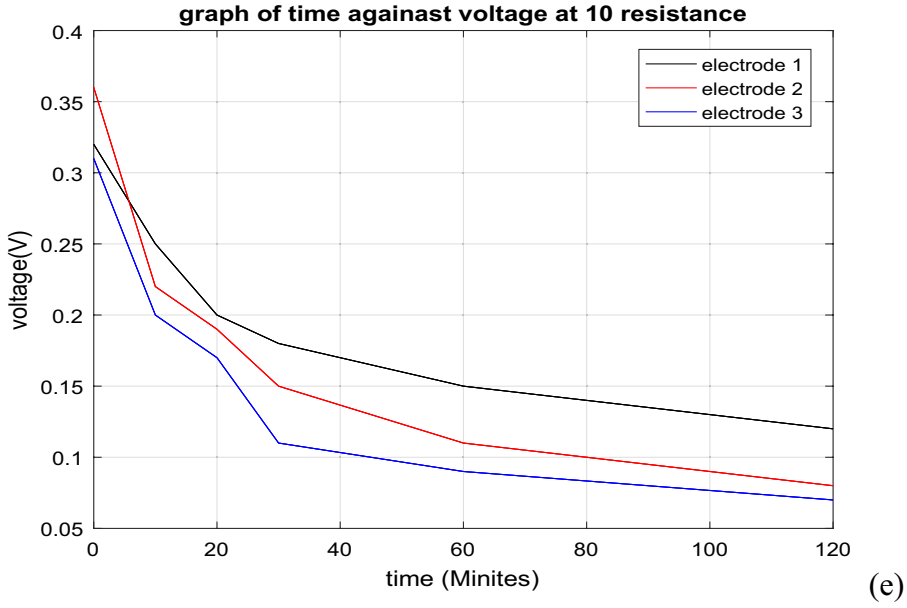

Fig. 8 (continued)

From Table 4, increasing the electrode amount is expected to linearly increase the energy density despite there being a minimal increment in the weight of the cells. The moderately low specific gravity of citric acid electrolyte (1.24 g/ml) further ensures the cells are more portable while maintaining high energy production.

4 Conclusions

The study demonstrated that it was possible to fabricate an Aluminium-citrate cell and effectively use it to store energy. The synthesized Al^{3+} electrodes (from Al_2O_3 nanoparticle) were found to have desirable morphological, phase and composition traits to enhance conductivity. Additionally, the citric acid from the *Dovyalis caffra* extracts complemented well with the electrodes as far as their morphologies were concerned. The fabricated cell indicated moderately high currents and slow discharge rates for varying electrode diameters and impedances. The study findings are quite promising in the Aluminium-ion cells for future green batteries. The cell's energy balance was 477.6–346.3 J/s, and its density was 47.1–53.7 Wh/kg. The results showed that the cells could successfully produce portable energy storage devices from waste materials. This research can be continued at controlled temperature and pressure to investigate their effect.

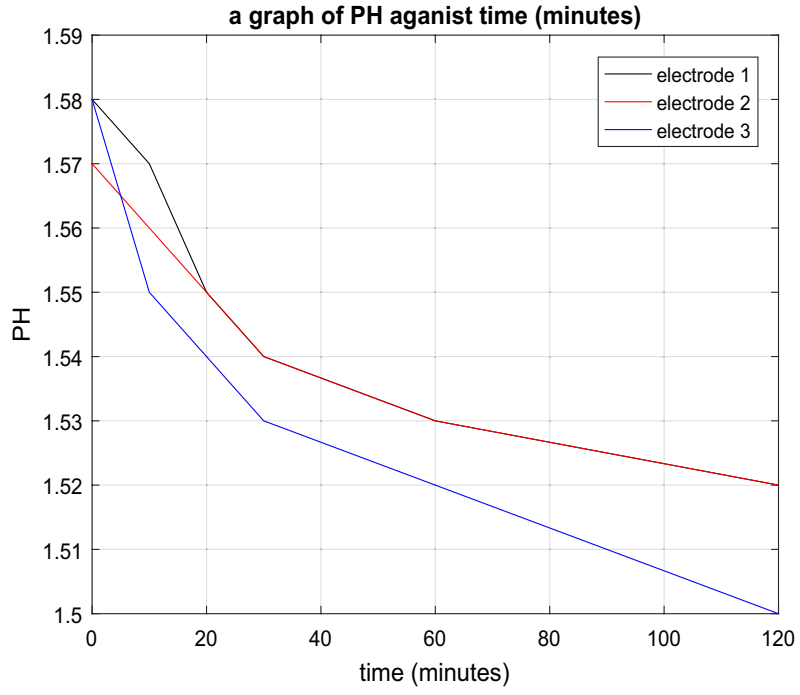

(a)

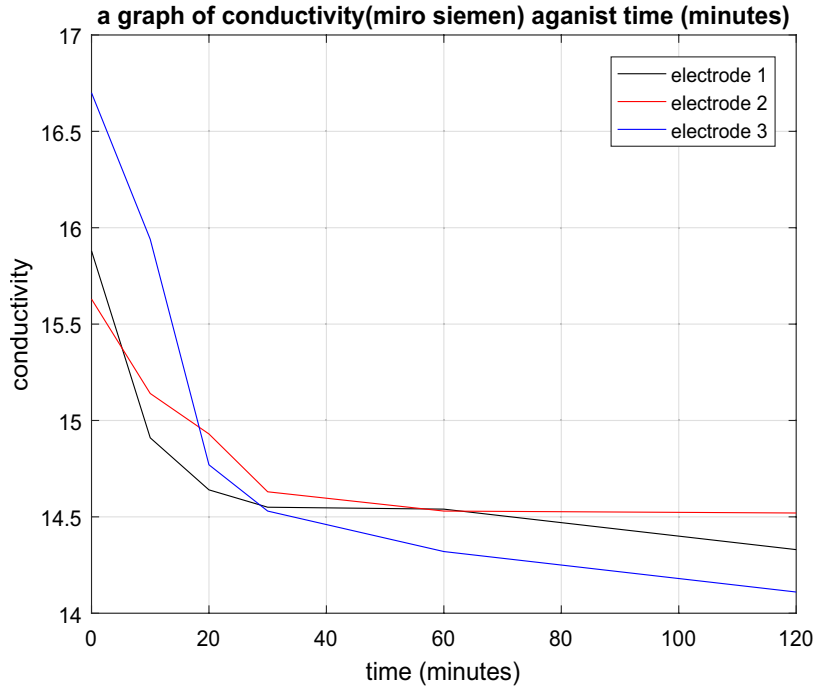

(b)

Fig. 9 Effects of the changes in electrolyte parameters where **a** is a graph of pH against time and **b** is a graph of conductivity against time. Where electrode 1, 2 and 3 had diameters of 2, 3 and 5 mm diameters respectively

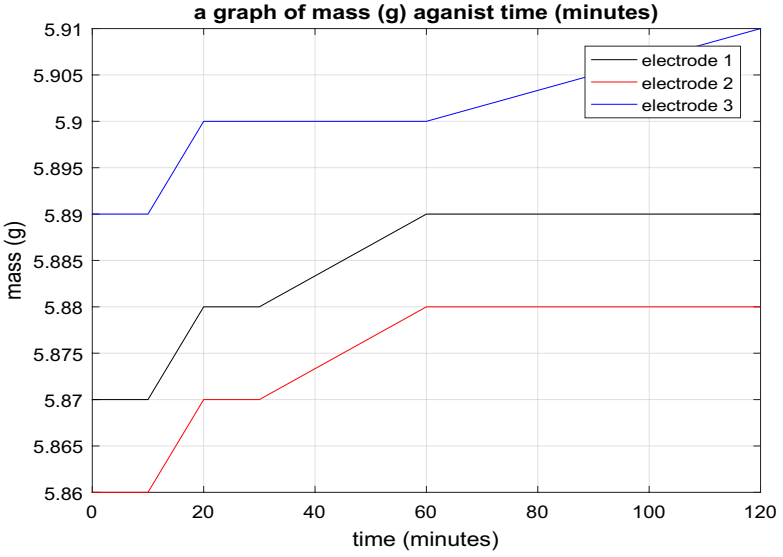

(a)

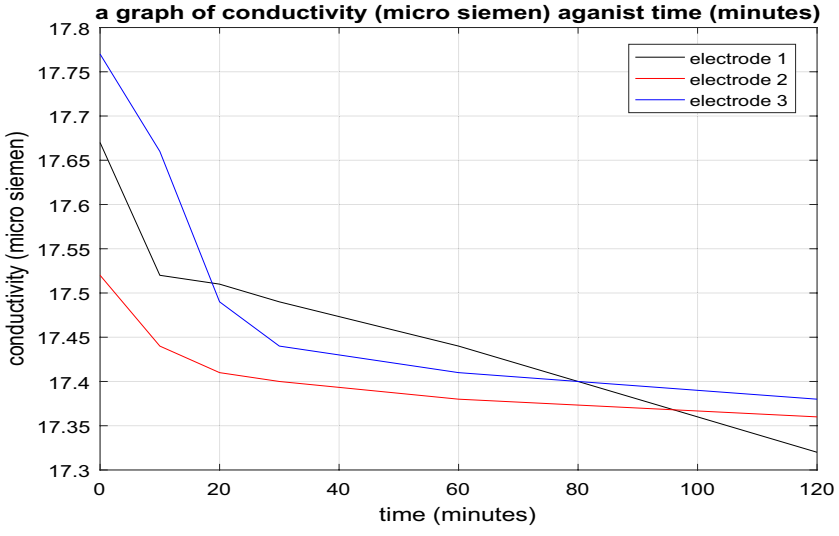

(b)

Fig. 10 Changes in electrode parameters **a** mass **b** conductivity **c** diameter **d** density with time. Where electrode 1, 2 and 3 had diameters of 2, 3 and 5 mm respectively

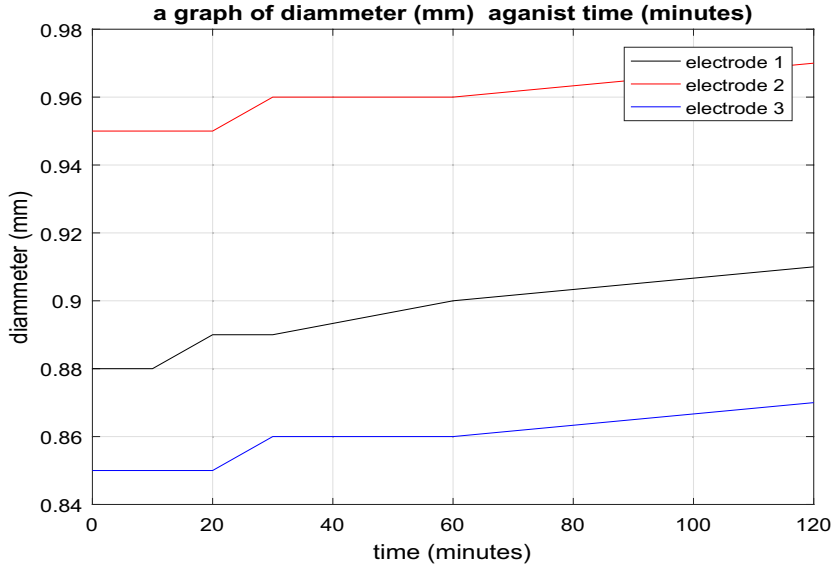

(c)

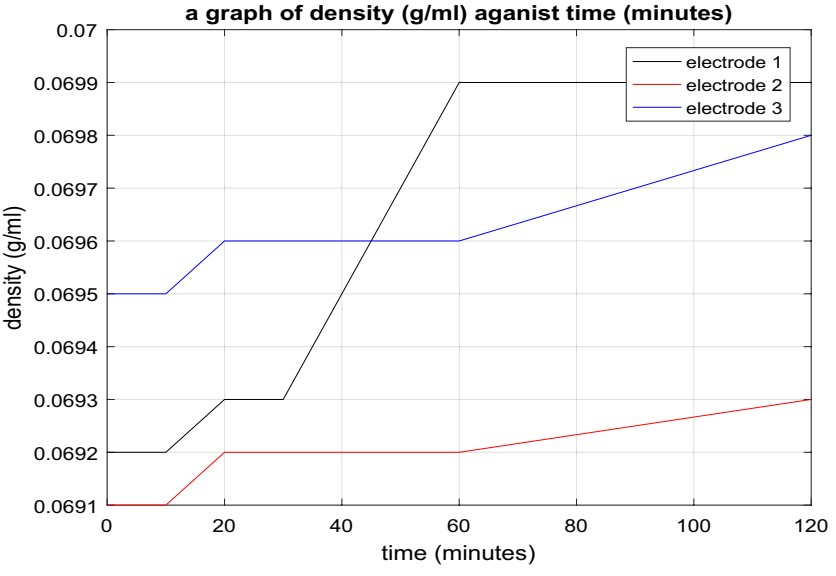

(d)

Fig. 10 (continued)

Table 4 The energy balance, capacity and density of the cells with various electrode diameters

Electrode diameter	Energy balance	Energy capacity	Gravimetric energy density	Volumetric energy density
2 mm	477.6 J/s	0.167 Wh/m^3	47.1 Wh/kg	38.0 Wh/ml
3 mm	540.5 J/s	0.189 Wh/m^3	53.3 Wh/kg	43.0 Wh/ml
5 mm	546.3 J/s	0.191 Wh/m^3	53.7 Wh/kg	43.3 Wh/ml

Abbreviations

FTIR Fourier transform infrared spectroscopy
SEM Scanning electron microscopy
EDS Energy dispersive X-ray spectroscopy
XRD X-ray diffraction

Acknowledgements

The authors acknowledge everyone who participated in this research. The experimental and characterization works were conducted at the Maasai Mara University Chemistry and Physics Laboratories, Narok-Kenya, Geology and Mines Kenya

Laboratories, Nairobi-Kenya, University of Witwatersrand, South Africa, Novosibirsk State university and Boreskov Institute of Catalysis, Russia.

Author contributions
John Wamumwe Mwangi —manuscript writing, revision and supervision Denis Kiragu- manuscript writing, revision and supervision Bakari chaka- manuscript writing, revision and supervision James Ndiritu- Revision.

Funding
This research did not receive funding from public, non-profit, commercial, or other grant sources.

Data availability
All the data associated with this research has been provided herein.

Declarations

Ethics and Consent to Participate declarations
We all agree with ethics and consent to participate declarations.

Consent for publication
Not applicable.

Competing interests
The authors declare no competing interests.

Received: 1 February 2025 / Accepted: 20 March 2026
Published online: 02 April 2026

References

1. Tong F, Yuan M, Lewis NS, Davis SJ, Caldeira K. Effects of deep reductions in energy storage costs on highly reliable wind and solar electricity systems. iScience. 2020. https://doi.org/10.1016/j.isci.2020.101484.
2. Wang W, et al. A new cathode material for super-valent battery based on aluminium ion intercalation and deintercalation. Sci Rep. 2013;3(1):3383. https://doi.org/10.1038/srep03383.
3. Backhaus R. Battery raw materials - where from and where to? ATZ Worldw. 2021;123(9):8–13. https://doi.org/10.1007/s38311-021-0715-5.
4. Padamata SK, Yasinskiy A, Polyakov PA. A review of secondary aluminum production and its byproducts. JOM. 2021;73:2603–14. https://doi.org/10.1007/s11837-021-04802-y.
5. Siddiqua A, Hahladakis JN, Al-Attiya WAKA. An overview of the environmental pollution and health effects associated with waste landfilling and open dumping. Environ Sci Pollut Res. 2022;29(39):58514–36. https://doi.org/10.1007/s11356-022-21578-z.
6. Ehsan F, Benjamin N, Dillon H, William M. Practical assessment of the performance of aluminium battery technologies. Nat Energy. 2021;6(1):21–9. https://doi.org/10.1038/s41560-020-00728-y.
7. William H, Geoffrey H, Jeffry M, Ralph P. General chemistry: Principles and modern applications. 9th ed. Upper Saddle River: Pearson Prentice Hall; 2007.
8. Schmidt-Rohr K. How Batteries store and release energy: Explaining basic electrochemistry. Chem Educ. 2018;95(10):1801–10. https://doi.org/10.1021/acs.jchemed.8b00479.
9. Kosar M, Taimoory SM, Diesenhaus O, Trant JF. Improvement of electrolytes for aluminum ion batteries: a molecular dynamics study. J Chem Phys. 2023;159(14):144503. https://doi.org/10.1063/5.0166001.
10. Zhu G, et al. Rechargeable aluminum batteries: effects of cations in ionic liquid electrolytes. RSC Adv. 2019;9(20):11322–30. https://doi.org/10.1039/C9RA00765B.
11. Martin WA. Electrochemical Deposition in Energy Storage Devices. Graduate Theses and Dissertations. 2021 Retrieved from https://scholarworks.uark.edu/etd/4228
12. Guduru RK, Icaza JC. A brief review on multivalent intercalation batteries with aqueous electrolytes. Nanomaterials. 2016;6(3):3. https://doi.org/10.3390/nano6030041.
13. Kravchyk KV, Kovalenko MV. Aluminum electrolytes for Al dual-ion batteries. Commun Chem. 2020;3(1):1–9. https://doi.org/10.1038/s42004-020-00365-2.
14. Nduni MN, Osano AM, Chaka B. Synthesis and characterization of aluminium oxide nanoparticles from waste aluminium foil and potential application in aluminium-ion cell. Clean Eng Technol. 2021;3:100108. https://doi.org/10.1016/j.clet.2021.100108.
15. Gesing TM, Robben L. Determination of the average crystallite size and the crystallite size distribution: the envelope function approach EnvACS. J Appl Crystallogr. 2024;57(5):5. https://doi.org/10.1107/S1600576724007362.
16. Donnelly MI, Dagley S. Bacterial degradation of 3,4,5-trimethoxycinnamic acid with production of methanol. J Bacteriol. 1981;147(2):471–6. https://doi.org/10.1128/jb.147.2.471-476.1981.
17. David WIF. Powder diffraction: By decades. In: Kolb U, Shankland K, Meshi L, Avilov A, David WIF, editors. Uniting electron crystallography and powder diffraction. Dordrecht: Springer; 2012. p. 3–14.
18. Li Z, et al. Aluminum oxide nanoparticle films deposited from a nonthermal plasma: synthesis, characterization, and crystallization. ACS Omega. 2020;5(38):24754–61. https://doi.org/10.1021/acsomega.0c03353.
19. Ates M, Demir V, Arslan Z, Daniels J, Farah IO, Bogatu C. Evaluation of alpha and gamma aluminum oxide nanoparticle accumulation, toxicity, and depuration in *Artemia salina* larvae. Environ Toxicol. 2015;30(1):109–18. https://doi.org/10.1002/tox.21917.
20. Vailionis A, Gamaly EG, Mizeikis V, Yang W, Rode AV, Juodkazis S. Evidence of superdense aluminium synthesized by ultrafast microexplosion. Nat Commun. 2011;2(1):445. https://doi.org/10.1038/ncomms1449.

21. Bagwell RB, Messing GL, Howell PR. The formation of α-Al_2O_3 from θ-Al_2O_3: the relevance of a 'critical size' and: diffusional nucleation or 'synchro-shear'? J Mater Sci. 2001;36(7):1833–41. https://doi.org/10.1023/A:1017545213590.
22. de Santos PS, Coelho ACV, de Santos HS, Kiyohara PK. Hydrothermal synthesis of well-crystallised boehmite crystals of various shapes. Mater Res. 2010;12:437–45. https://doi.org/10.1590/S1516-14392009000400012.
23. Krewski D, et al. Human health risk assessment for aluminium, aluminium oxide, and aluminium hydroxide. J Toxicol Environ Health Part B. 2007;10(sup1):1–269. https://doi.org/10.1080/10937400701597766.
24. Conroy M, et al. Importance of interlayer H bonding structure to the stability of layered minerals. Sci Rep. 2017;7(1):13274. https://doi.org/10.1038/s41598-017-13452-7.
25. Moser D, et al. Corrosion of passive aluminum anodes in a chloroaluminate deep eutectic solvent for secondary batteries: the bad, the good, and the ugly. ACS Appl Mater Interfaces. 2023;15(1):882–92. https://doi.org/10.1021/acsami.2c16153.
26. Wu R, Yu Y, Jia S, Zhou C, Cojocaru-Mirédin O, Wuttig M. Strong charge carrier scattering at grain boundaries of PbTe caused by the collapse of metavalent bonding. Nat Commun. 2023;14(1):719. https://doi.org/10.1038/s41467-023-36415-1.
27. Benny L, Cherian AR, Varghese A, Hegde G. Recent developments on electrochemical sensing applications using vegetable fiber based porous carbon materials. In: Jawaid M, Khan A, editors. Vegetable fiber composites and their technological applications. Singapore: Springer; 2021. p. 107–26.
28. Mohamed HFM, Abdel-Hady EE, Abdel-Moneim MMY, Bakr MAM, Soliman MAM, Shehata MGH, et al. Effect of Al_2O_3 on nanostructure and ion transport properties of PVA/PEG/SSA polymer electrolyte membrane. Polymers. 2022;14:4029. https://doi.org/10.3390/polym14194029.
29. Manimegalai P. Green synthesis of zinc oxide (ZnO) nanoparticles using aqueous leaf extract of *Hardwickia binata*: their characterizations and biological applications. Biomass Conv Bioref. 2024;14(11):12559–74. https://doi.org/10.1007/s13399-023-04279-6.
30. Prorok R, Ramult J, Nocun-Wczelik W, Madej D. The effect of chelate compounds on the hydration process of MgO–Al_2O_3 phase system under hydrothermal conditions. Appl Sci. 2021;11(6):Art. no. 6. https://doi.org/10.3390/app11062834.
31. Waweru DM, Arimi JM, Marete E, Jacquier J-C, Harbourne N. Current status of utilization and potential of *Dovyalis caffra* fruit: major focus on Kenya - a review. Sci Afr. 2022;16:e01097. https://doi.org/10.1016/j.sciaf.2022.e01097.
32. Rago L, et al. Influences of dissolved oxygen concentration on biocathodic microbial communities in microbial fuel cells. Bioelectrochemistry. 2017;116:39–51. https://doi.org/10.1016/j.bioelechem.2017.04.001.
33. Wang Y, et al. Electrolyte engineering enables high performance zinc-ion batteries. Small. 2022;18(43):2107033. https://doi.org/10.1002/smll.202107033.
34. Wei Y, Jiao Y, An D, Li D, Li W, Wei Q. Review of dissolved oxygen detection technology: from laboratory analysis to online intelligent detection. Sensors. 2019;19(18):Art. no. 18. https://doi.org/10.3390/s19183995.
35. Zhao Y, et al. Solid polymer electrolytes with high conductivity and transference number of Li ions for Li-based rechargeable batteries. Adv Sci. 2021;8(7):2003675. https://doi.org/10.1002/advs.202003675.
36. Rahimnejad M. Chapter 5 - Energy and power measurement methods in MFCs. In: Rahimnejad M, editor. Biological fuel cells. Amsterdam: Elsevier; 2023. p. 127–46.
37. Fish RM, Geddes LA. Conduction of electrical current to and through the human body: a review. Eplasty. 2009;9:e44.
38. Dong Y, et al. Multi-functional nanocellulose based nanocomposites for biodegradable food packaging: Hybridization, fabrication, key properties and application. Carbohydr Polym. 2023;321:121325. https://doi.org/10.1016/j.carbpol.2023.121325.
39. Wu Q, Liu J, Li Q, Mo W, Wan R, Peng S. Effect of electrode distances on remediation of eutrophic water and sediment by sediment microbial fuel cell coupled floating beds. Int J Environ Res Public Health. 2022;19(16):Art. no. 16. https://doi.org/10.3390/ijerph191610423.
40. Akinyemi AS, Musasa K, Davidson IE. Analysis of voltage rise phenomena in electrical power network with high concentration of renewable distributed generations. Sci Rep. 2022;12(1):7815. https://doi.org/10.1038/s41598-022-11765-w.
41. Sedlák P, Kuberský P. The effect of the orientation towards analyte flow on electrochemical sensor performance and current fluctuations. Sensors. 2020;20(4):Art. no. 4. https://doi.org/10.3390/s20041038.
42. Yermoshin NI, Yakimov EV, Goldshtein AE, Sednev DA. Increase in fast response time of the resistance-to-voltage converter when monitoring the cable products' insulation resistance. Sensors. 2021;21(2):Art. no. 2. https://doi.org/10.3390/s21020368.
43. Zhang W, Chen X, Wang Y, Wu L, Hu Y. Experimental and modeling of conductivity for electrolyte solution systems. ACS Omega. 2020;5(35):22465–74. https://doi.org/10.1021/acsomega.0c03013.
44. Schweiger H-G, et al. Comparison of several methods for determining the internal resistance of lithium ion cells. Sensors. 2010;10(6):Art. no. 6. https://doi.org/10.3390/s100605604.
45. Jesudason CG. Broad considerations concerning electrochemical electrodes in primarily fluid environments. Int J Mol Sci. 2009;10(5):Art. no. 5. https://doi.org/10.3390/ijms10052203.
46. Wang V, Zeng S, Guo J, Qin T. Remaining capacity estimation of lithium-ion batteries based on the constant voltage charging profile. PLoS ONE. 2018;13(7):e0200169. https://doi.org/10.1371/journal.pone.0200169.
47. Nakata S. Investigation of charging efficiency of a lithium-ion capacitor during galvanostatic charging method. Materials. 2019;12(19):3191. https://doi.org/10.3390/ma12193191.
48. Thiong'o B, Osano A, Bakari C. Investigating the Ohmic behavior of mediator-less microbial fuel cells using sewerage water as the bio-anode. Cogent Eng. 2022;9(1):2079222. https://doi.org/10.1080/23311916.2022.2079222.
49. Lira RB, Leomil FSC, Melo RJ, Riske KA, Dimova R. To close or to collapse: The role of charges on membrane stability upon pore formation. Adv Sci. 2021;8(11):e2004068. https://doi.org/10.1002/advs.202004068.

Publisher's Note